NEU PRESS

ASREL Aerospace Research Letters

Volume: 4 Issue: 2 Year: 2025 Research Article e-ISSN: 2980-0064

# Fault Tolerant Control of an Octoplane UAV Using Sliding Mode Methods

**İbrahim Mızrak[1*] Halim Alwi[1] Christopher Edwards[1]**

[1] University of Exeter, Faculty of Environment, Science and Economy, Engineering Department, Exeter, the United Kingdom

**Article Info**

**Received:** 11.07.2025
**Accepted:** 25.08.2025
**Published:** 31.12.2025

**Keywords:**
Dual-systems,
Octoplane UAVs,
Hybrid UAVs,
Sliding mode control,
Fault tolerant control.

**ABSTRACT**

This article presents a Fault Tolerant Control (FTC) scheme for an octoplane UAV, a fixed-wing unmanned aerial vehicle equipped with eight vertical rotors, using sliding mode control (SMC) allocation. The proposed approach requires the design of only a single baseline controller that is effective under fault-free and fault/failure scenarios. The scheme fully exploits the octoplane's redundant vertical rotors and additional control surfaces, including the elevator, rudder, and independently operated ailerons, to manage total actuator faults/failures during cruise flight. The approach utilises sliding mode control with a control allocation (CA) strategy to redistribute control signals in the event of actuator failure. Simulation results based on a nonlinear model of the octoplane are presented at the end of the article to demonstrate the effectiveness of the proposed scheme. The simulation results demonstrate that the proposed scheme maintains tracking accuracy within ±1% error under fault-free conditions. Despite coupling effects, it achieves over 95% tracking performance even in the case of actuator faults and failures.

## Octoplane İHA'nın Kayar Kipli Yöntem Kullanarak Hata Toleranslı Kontrolü

**Makale Bilgisi**

**Geliş Tarihi:** 11.07.2025
**Kabul Tarihi:** 25.08.2025
**Yayın Tarihi:** 31.12.2025

**Anahtar Kelimeler:**
Çift sistemler,
Octoplana İHAlar,
Hibrit İHAlar,
Kayar kipli kontrol,
Hata dayanımlı kontrol.

**ÖZET**

Bu makale, sekiz adet dikey rotora sahip sabit kanatlı bir insansız hava aracı olan octoplane İHA için kayan kipli kontrol (SMC) temelli bir Arıza Toleranslı Kontrol (FTC) yöntemi sunmaktadır. Önerilen yaklaşım, hem arızasız koşullarda hem de çeşitli aktüatör arıza ve hata senaryolarında etkinliğini koruyan tek bir temel (baseline) denetleyicinin tasarlanmasını gerektirir. Kontrol yapısı, octoplane İHA'nın yedekli dikey rotorları ile ilave kontrol yüzeyleri—elevatör, rudder ve bağımsız olarak çalışabilen aileronlar—aracılığıyla seyir uçuşu sırasında meydana gelebilecek tam aktüatör arızalarının üstesinden gelebilmektedir. Bu yöntem, aktüatör kayıpları durumunda kontrol sinyallerini yeniden dağıtmak amacıyla kayma kipi kontrolünün dayanıklılığını ve kontrol paylaştırma (CA) stratejisini birlikte kullanmaktadır. Octoplane'in doğrusal olmayan bir modeli üzerinde gerçekleştirilen simulasyon sonuçları, önerilen yöntemin etkinliğini göstermek üzere makalenin sonunda sunulmaktadır. Simülasyon sonuçları, önerilen yöntemin hatasız koşullarda ±%1 hatalı doğrulukla izleme başarımını koruduğunu göstermektedir. Coupling etkilerine rağmen, aktüatör arızaları ve kayıpları durumunda dahi %95'in üzerinde izleme performansı sağlamaktadır.

**To cite this article:**

Mızrak, İ., Alwi, H., Edwards, C. (2025). Fault Tolerant Control of an Octoplane UAV Sliding Mode Method. *Aerospace Research Letters (ASREL), 4*(2), 223-251.

*** Corresponding Author:** İbrahim Mızrak, *ibrahim.mizrak@windowslive.com, ibrahim.mizrak@erbakan.edu.tr*

## INTRODUCTION

In recent years, unmanned aerial vehicles (UAVs), commonly known as drones, have gained considerable attention due to offering versatile and cost-effective solutions across a growing range of applications, including military missions, search and rescue operations, passenger transportation, aerial mapping, medical deliveries, construction monitoring, and parcel transport (Dağ. et al., 2023; Mohsan et al., 2022; Varlık & Erdönmez, 2020; Saeed et al., 2018).

Compared to manned aircraft, UAVs can be employed in hazardous missions without risking pilot safety. However, their loss rates have been reported to be up to ten times higher than those of manned aircraft for these missions (Sadeghzadeh & Zhang, 2011). Moreover, UAV accidents may cause environmental damage, structural destruction, financial loss, or even fatalities. These challenges highlight the importance of fault-tolerant control (FTC) to enhance UAV reliability and have motivated extensive research in recent years (Sadeghzadeh, 2015).

UAVs are generally categorised into two main types: multirotor UAVs, such as quadcopters, and fixed-wing UAVs. Both groups have benefits depending on the intended application. While multirotor UAVs do not require runways and are capable of hovering and, have greater manoeuvrability, fixed-wing UAVs offer longer endurance and higher payload capacity (Ducard & Allenspach, 2021; Saeed et al., 2015). To combine the advantages of both configurations, hybrid UAVs, also known as fixed-wing VTOL UAVs, have been developed (Ducard & Allenspach, 2021).

There are two main classes of hybrid UAV configurations, as shown in Figure 1 namely convertiplanes and tail-sitters. Convertiplanes maintain their airframe orientation during all flight phases with actuators reorienting to provide the required thrust. On the other hand, tail-sitters rotate their entire airframe from vertical to horizontal flight by keeping the thrusters fixed relative to the body frame (Saeed et al., 2018).

**Figure 1**
*Categorisation of hybrid UAVs according to design configurations (adapted from (Saeed et al., 2018))*

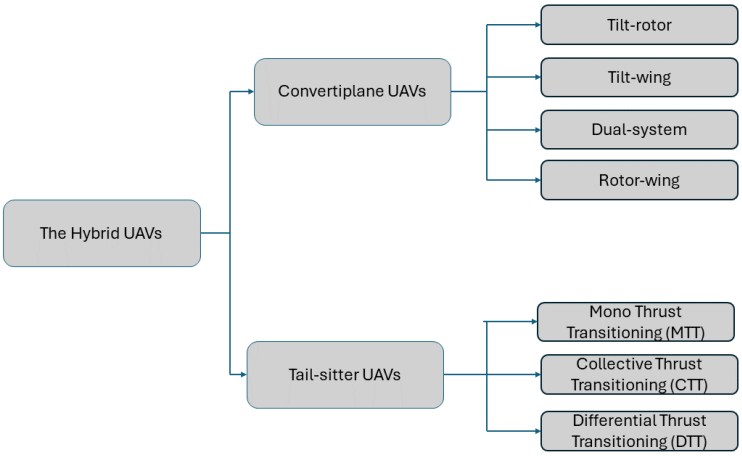


One type of convertiplane UAVs is the dual-system configuration (see the examples in Figure 2). This configuration combines two separate sets of rotors: one dedicated to vertical take-off and landing (VTOL) and another for forward cruise flight. During hover, the UAV exhibits dynamic characteristics similar to those of multi-rotor systems. The transition phase begins with the activation of the forward propeller. Upon reaching cruise speed, the vertical rotors are deactivated, and the UAV operates as a fixed-wing aircraft. The dual-system features a straightforward mechanical design, which facilitates ease of manufacturing and maintenance, while also offering greater endurance compared to other convertiplane UAV configurations. It also provides relatively simple controllability and stabilisation

during take-off and landing phases (Gu et al., 2017)**.** However, the configuration presents certain drawbacks, including increased aerodynamic drag and additional weight resulting from the forward propulsion system. Despite these drawbacks, the dual-system offers considerable applicable advantages, making it a promising option for future UAV development. Its popularity has grown considerably in recent years across both academic and industrial fields, as evidenced by increasing references in academic papers (Munasinghe & Gunarathna, 2018; Prochazka et al., 2019; Yu & Kwon, 2017) and industry publications (Anon, 2018, 2019, 2023; Bothge, 2022; Team, 2022; Technologies, 2024).

Dual-system UAVs are typically classified into different categories depending on the number of vertical rotors: combined helicopter (Heredia et al., 2012), bi-rotor (Pocock, 2012), quadrotor (Technologies, 2024) and octorotor platforms (Honda Motor Co., Ltd., 2022). Despite their benefits, dual-system UAVs with fewer than six vertical rotors exhibit limited FTC capability due to the lack of actuator redundancy. A total failure of any rotor may lead to the loss of control and cause the UAV to crash (Khattab et al., 2024). Therefore, UAVs with six or more rotors offer considerable advantages in handling faults or failures. There are a few studies in the literature that address over-actuated systems (see, for example, (Cai & Lovera, 2024; Ijaz et al., 2024; Murphy et al., n.d.)**.**

Furthermore, the investigations by major companies such as Honda (Honda Motor Co., Ltd., 2022), Volkswagen (Bothge, 2022), and Wisk (Wisk, 2024) into urban air mobility solutions (as illustrated in Figure 2) demonstrate the adaptability of dual-system configurations for passenger transportation ‘drone taxis’ using octoplane or dodecaplane UAVs, due to their considerable advantages in handling faults or failures. While the models developed by Honda and Volkswagen feature two forward propellers, Wisk’s model utilises a single forward propeller.

Sliding Mode Control (SMC) is a robust control method known for its effectiveness against so-called ‘matched’ uncertainties (Edwards & Spurgeon, 1998). This robustness has made SMC an attractive approach for Fault-Tolerant Control (FTC) in UAVs. However, there is limited research applying SMC-based FTC to hybrid UAVs, and a few exceptions for octoplane UAVs (e.g., (Ijaz et al., 2024; Mizrak et al., 2021)).

Unlike other categories, octoplane UAVs offer notable advantages in terms of redundancy and control capability, especially under fault/failure conditions. As over-actuated systems, octoplanes incorporate four additional vertical rotors, allowing them to maintain full attitude control even in the case of up to four rotor failures.

The primary motivation of this study is to address these challenges by developing a fault-tolerant control (FTC) strategy based on sliding mode control (SMC), specifically designed for the octoplane UAV to ensure reliable performance even under fault and failure conditions. This paper begins with the development of the equations of motion for the octoplane, followed by the design of the FTC scheme and finally a presentation of the simulation results.

**Figure 2**
*Dual-system UAVs: a) Example of a quadplane (adapted from (Zhou et al., 2023)), b) Octoplane – Honda eVTOL Vol. 2 (adapted from (Honda Motor Co., Ltd., 2022)), c) Dodecaplane – Wisk Aero Cora (Gen 5) (adapted from (Wisk, 2024)).*

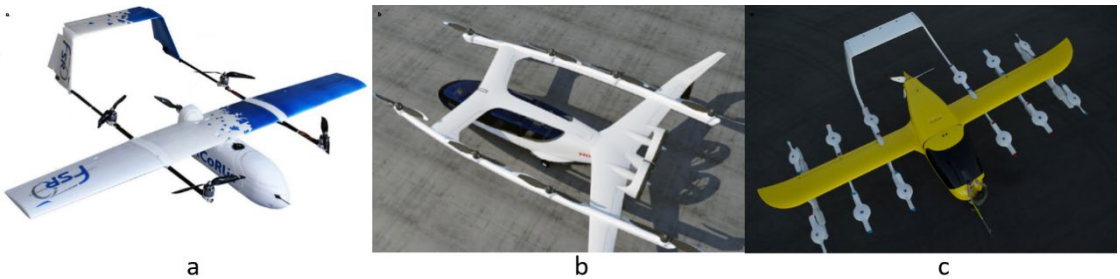

a b c

**Equation of Motion of the Octoplane**

This section presents the equations of motion for the octoplane considered in this study. Twelve main equations of motion, involving both force and moment equations, are introduced. The octoplane considered here is a modified version of the traditional fixed-wing UAV, the Aerosonde, reconfigured into a hybrid dual-system UAV with eight vertical rotors. The aerodynamic coefficients for the Aerosonde, shown in Table 1, are taken from (Beard & McLain, 2012)**.**

Figure 3 shows the octoplane used in this study possessing eight vertical rotors and various more traditional control surfaces. The UAV features two ruddervators, positioned on the left and right of the tail, which serve dual functions: symmetric deflections act as elevators to control pitch, while anti-symmetric deflections act as a rudder to control yaw. In addition, two independently operated ailerons are used to control the roll motion.

The problem formulation and assumptions used in the design process are based on (Beard & McLain, 2012; Kringeland, 2019; Köprücü & Öztürk, 2024).

- The octoplane is modelled as a rigid body with constant mass.
- The octoplane is geometrically symmetric about the body's *xz*-plane.
- The vertical rotors are aligned with the body's *z*-axis and symmetrically positioned to the *xz*-plane.
- Wind effects are neglected, indicating that the airspeed ($V_a$) (m/s) is equal to the ground speed ($V_g$) (m/s) , and corresponds to the true airspeed ($V_{tas}$) (m/s).
- Flaps are not included in the control design, and therefore, it is neglected.
- Actuator dynamics are not modelled, and it is assumed that actuators respond instantaneously.
- The pusher propeller motor is inclined by 1 degree ($\kappa$) relative to the aircraft longitudinal axis ($x_b$) (see Figure 3 and Figure 4)

**Figure 3**
*The configuration and rotation directions of the vertical rotors and the control surfaces of the octoplane UAV.*

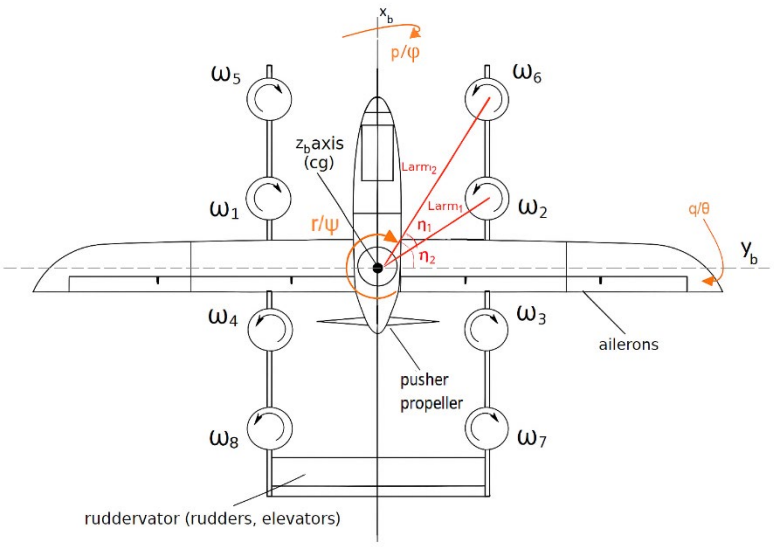


**Figure 4**
*The side view of the octoplane*

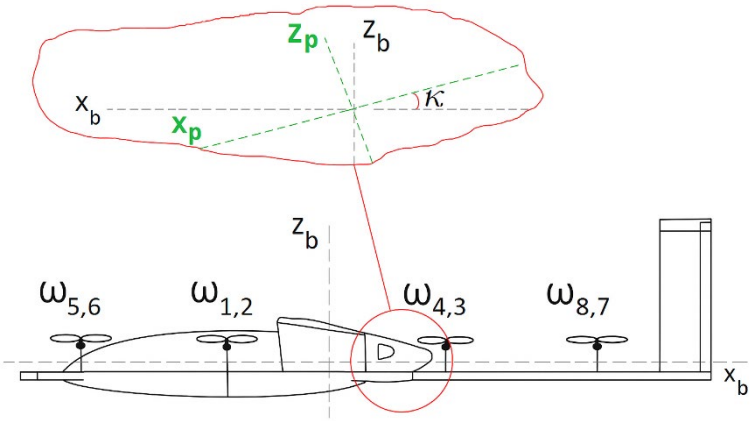


The 12 state variables governing the dynamical system of the octoplane, as shown in Figure 2, are given by (Beard & McLain, 2012)

$$\dot{\phi} = p + \sin\phi\tan\theta \cdot q + \cos\phi\tan\theta \cdot r \tag{1}$$

$$\dot{\theta} = \cos\phi \cdot q - \sin\phi \cdot r \tag{2}$$

$$\dot{\psi} = \frac{\sin\phi}{\cos\theta} \cdot q + \frac{\cos\phi}{\cos\theta} \cdot r \tag{3}$$

$$\dot{p} = \Gamma_1 pq - \Gamma_2 qr + \Gamma_3 \mathcal{L} + \Gamma_4 \mathcal{N} + \frac{J_r}{J_{xx}} q\omega_r \tag{4}$$

$$\dot{q} = \Gamma_5 pr - \Gamma_6 (p^2 - r^2) + \frac{1}{J_{yy}} \mathcal{M} - \frac{J_r}{J_{yy}} p\omega_r \tag{5}$$

$$\dot{r} = \Gamma_7 pq - \Gamma_1 qr + \Gamma_4 \mathcal{L} + \Gamma_8 \mathcal{N} \tag{6}$$

$$\dot{u} = rv - qw + \frac{1}{m} f_x \tag{7}$$

$$\dot{\mathcal{V}} = r\mathcal{V} - q\mathcal{W} + \frac{1}{m}f_x \tag{8}$$

$$\dot{\mathcal{W}} = \mathcal{W} - r\mathcal{U} + \frac{1}{m}f_y \tag{9}$$

The rate of change of position in the inertial frame is given by

$$\begin{bmatrix}\dot{x}\\ \dot{y}\\ \dot{z}\end{bmatrix} = \begin{bmatrix}\cos\theta\cos\psi & \sin\phi\sin\theta\cos\psi - \cos\phi\sin\psi & \cos\phi\sin\theta\cos\psi + \sin\phi\sin\psi\\ \cos\theta\sin\psi & \sin\phi\sin\theta\sin\psi + \cos\phi\cos\psi & \cos\phi\sin\theta\sin\psi - \sin\phi\cos\psi\\ \sin\theta & \sin\phi\cos\theta & \cos\phi\cos\theta\end{bmatrix}\begin{bmatrix}\mathcal{V}\\ \mathcal{U}\\ \mathcal{W}\end{bmatrix} \tag{10}$$

The state variables are

- roll, pitch, and yaw angles: $\phi, \theta, \psi$ (rad)
- roll, pitch, and yaw rates: $p, q, r$ (rad/s)
- linear velocities in the body frame: $\mathcal{U}, \mathcal{V}, \mathcal{W}$ (m/s)
- UAV positions in the inertial frame: $x, y, z$ (m)

The variable $J_r$ appearing in (4) and (5) represents the inertia moment of the vertical rotors, while $\omega_r$ (rad/s) is the total residual vertical rotor speed, defined by

$$\omega_r = -\omega_1 - \omega_2 + \omega_3 + \omega_4 - \omega_5 - \omega_6 + \omega_7 + \omega_8 \tag{11}$$

The moment of inertia of the octoplane is defined by

$$\boldsymbol{J} = \begin{bmatrix}J_{xx} & 0 & -J_{xz}\\ 0 & J_{yy} & 0\\ -J_{xz} & 0 & J_{zz}\end{bmatrix} \tag{12}$$

To simplify the notation in (4)-(6), the following constants are defined

$$\begin{aligned}
\Gamma_1 &= \frac{J_{xz}\left(J_{xx} - J_{yy} + J_{zz}\right)}{\Gamma_0},\\
\Gamma_2 &= \frac{J_{zz}\left(J_{zz} - J_{yy}\right) + J_{xz}^2}{\Gamma_0},\\
\Gamma_3 &= \frac{J_{zz}}{\Gamma_0},\\
\Gamma_4 &= \frac{J_{xz}}{\Gamma_0},\\
\Gamma_5 &= \frac{J_{zz} - J_{xx}}{J_{yy}},\\
\Gamma_6 &= \frac{J_{xz}}{J_{yy}},\\
\Gamma_7 &= \frac{J_{xx}\left(J_{xx} - J_{yy}\right) + J_{xz}^2}{\Gamma_0},\\
\Gamma_8 &= \frac{J_{xx}}{\Gamma_0},\\
\Gamma_0 &= J_{xx}J_{zz} - J_{xz}^2
\end{aligned} \tag{13}$$

Based on the standard formulation in (Beard & McLain, 2012), and incorporating the forward motor inclined as well as the additional force generated by the eight vertical rotors, the total external forces acting on the aircraft can be expressed as follows:

$$f_x = -mg\sin\theta + \frac{1}{2}\rho_{air}V_{tas}^2 S_{aero}\left[-\left(C_{D_0} + C_{D_\alpha}\alpha\right)\cos\alpha + \left(C_{L_0} + C_{L_\alpha}\alpha\right)\sin\alpha + \left(-C_{D_q}\cos\alpha + C_{L_q}\sin\alpha\right)\frac{cq}{2V_{tas}} + \left(-C_{D_{\delta_e}}\cos\alpha + C_{L_{\delta_e}}\sin\alpha\right)\delta_e\right] + \delta_T\cos\kappa \quad (14)$$

$$f_y = mg\sin\phi\cos\theta + \frac{1}{2}\rho_{air}V_{tas}^2 S_{aero}\left[C_{Y_0} + C_{Y_\beta}\beta + C_{Y_p}\frac{bp}{2V_{tas}} + C_{Y_r}\frac{br}{2V_{tas}} + C_{Y_{\delta_a}}\delta_a + C_{Y_{\delta_r}}\delta_r\right] \quad (15)$$

$$f_z = mg\cos\phi\cos\theta + \frac{1}{2}\rho_{air}V_{tas}^2 S_{aero}\left[-\left(C_{D_0} + C_{D_\alpha}\alpha\right)\sin\alpha - \left(C_{L_0} + C_{L_\alpha}\alpha\right)\cos\alpha + \left(-C_{D_q}\sin\alpha - C_{L_q}\cos\alpha\right)\frac{cq}{2V_{tas}} + \left(-C_{D_{\delta_e}}\sin\alpha - C_{L_{\delta_e}}\cos\alpha\right)\delta_e\right] - \delta_T\sin\kappa + F_{T_z} \quad (16)$$

where the variables $C_L, C_D, C_Y$ are dimensionless standard aerodynamic coefficients. Furthermore, the various parameters used in (14)-(16) are given as follows: $\rho_{air}$ denotes the air density (kg/m$^3$), $S_{aero}$ is the aerodynamic surface area (m$^2$), $V_{tas}$ represents the true airspeed (m/s), $c$ is the mean chord length of the aerofoil (m), and $\beta$ is the sideslip angle (rad).

The total external moments (Nm) acting on the aircraft are defined by (Beard & McLain, 2012)

$$\mathcal{L} = \tau_{\text{roll}} + \frac{1}{2}\rho_{air}V_{tas}^2 S_{aero} b\left(C_{l_0} + C_{l_\beta}\beta + C_{l_p}\frac{b}{2V_{tas}}p + C_{l_r}\frac{b}{2V_{tas}}r + C_{l_{\delta_a}}\delta_a + C_{l_{\delta_r}}\delta_r\right) \quad (17)$$

$$\mathcal{M} = \tau_{\text{pitch}} - \delta_T d\sin\kappa + \frac{1}{2}\rho_{air}V_{tas}^2 S_{aero} c\left(C_{m_0} + C_{m_\alpha}\alpha + C_{m_q}\frac{c}{2V_{tas}}q + C_{m_{\delta_e}}\delta_e\right) \quad (18)$$

$$\mathcal{N} = \tau_{\text{yaw}} + \frac{1}{2}\rho_{air}V_{tas}^2 S_{aero} b\left(C_{n_0} + C_{n_\beta}\beta + C_{n_p}\frac{b}{2V_{tas}}p + C_{n_r}\frac{b}{2V_{tas}}r + C_{n_{\delta_a}}\delta_a + C_{n_{\delta_r}}\delta_r\right) \quad (19)$$

where the variables $\tau_{roll}, \tau_{pitch}, \tau_{yaw}$ define the roll, pitch, and yaw moments produced by the vertical rotors, while the dimensionless aerodynamic coefficients for the pitch, roll and yaw moments are denoted by $C_m, C_l, C_n$, respectively. Additionally, $d$ is the distance between the UAV's centre of gravity and the centre of the pusher propeller (m).

According to (Beard & McLain, 2012), the true airspeed ($V_{tas}$) (m/s), angle of attack ($\alpha$) (rad) and sideslip angle ($\beta$) (rad) can be determined under the conditions $\mathcal{U} > 0$ and $V_{tas} \neq 0$ according to

$$V_{tas} = \sqrt{\mathcal{U}^2 + \mathcal{V}^2 + \mathcal{W}^2} \quad (20)$$

$$\alpha = tan^{-1}\left(\frac{\mathcal{W}}{\mathcal{U}}\right) \quad (21)$$

$$\beta = sin^{-1}\left(\frac{\mathcal{V}}{V_{tas}}\right) \quad (22)$$

The thrust and torques produced by the vertical rotors are defined by

$$\underbrace{\begin{bmatrix} F_{T_x} \\ F_{T_y} \\ F_{T_z} \\ \tau_{roll} \\ \tau_{pitch} \\ \tau_{yaw} \end{bmatrix}}_{\tau} = \underbrace{\begin{bmatrix} 0 & 0 & 0 & 0 & 0 & 0 & 0 & 0 \\ 0 & 0 & 0 & 0 & 0 & 0 & 0 & 0 \\ C_{T_q} & C_{T_q} & C_{T_q} & C_{T_q} & C_{T_q} & C_{T_q} & C_{T_q} & C_{T_q} \\ C_{T_q}l_1 & -C_{T_q}l_1 & -C_{T_q}l_1 & C_{T_q}l_1 & C_{T_q}l_3 & -C_{T_q}l_3 & -C_{T_q}l_3 & C_{T_q}l_3 \\ C_{T_q}l_2 & C_{T_q}l_2 & -C_{T_q}l_2 & -C_{T_q}l_2 & C_{T_q}l_4 & C_{T_q}l_4 & -C_{T_q}l_4 & -C_{T_q}l_4 \\ C_{M_q} & -C_{M_q} & C_{M_q} & -C_{M_q} & C_{M_q} & -C_{M_q} & C_{M_q} & -C_{M_q} \end{bmatrix}}_{B_\Omega} \underbrace{\begin{bmatrix} \Omega_1(t) \\ \vdots \\ \Omega_8(t) \end{bmatrix}}_{u_p} \quad (23)$$

where the vector $u_p$ denotes the control input to the vertical rotors with its $i$th component ($\Omega_i(t)$ ($rps^2$)) defined as

$$\Omega_i(t) = \omega_i(t)\ |\ \omega_i(t)\ | \quad (24)$$

where $\omega_i$ defines the angular rate of the $i$th rotor, and the matrix $B_\Omega$ includes the physical parameters of the vertical rotors, such as thrust and moment coefficients ($C_{T_q}$ and $C_{M_q}$), as well as the geometry of the

rotor layout. This matrix determines how the desired control actions are translated into specific rotor commands. Note that $F_{T_x}$ and $F_{T_y}$ are assumed to be zero, as there is no force generated by the vertical rotors along the *x- or y*-axes.

**The Model for Cruise Flight**

The nonlinear model defined in (1)-(22) is linearised to obtain a model to be used as the basis for the control design. These trimming and linearisation were carried out during cruise flight at an altitude of 1000 m using the *Simulink Linearization Tool* (MathWorks, 2024). The model was also tested in *FlightGear* and operated under the trim conditions obtained from the linearisation process to validate its stability. The integration with *FlightGear* was implemented by the author (for an example of a similar implementation, see (Kulaksız & Hançer, 2022)). The trimmed flight condition is given by the following state and input vectors:

***Velocity vector (m/s):***

$$\begin{bmatrix} u_0 \\ v_0 \\ w_0 \end{bmatrix} = \begin{bmatrix} 33.76 \\ 0 \\ 0.76 \end{bmatrix} (m/s) \tag{25}$$

***Attitude and Angular Rates (deg):***

$$\begin{bmatrix} \phi_0 \\ \theta_0 \\ \psi_0 \\ p_0 \\ q_0 \\ r_0 \\ \alpha_0 \\ \beta_0 \end{bmatrix} = \begin{bmatrix} 0 \\ 1.29 \\ 0 \\ 0 \\ 0 \\ 0 \\ 1.29 \\ 0 \end{bmatrix} (deg) \tag{26}$$

***Trimmed control inputs:***

$$\begin{bmatrix} \delta_{e1_0} \\ \delta_{e2_0} \\ \delta_{T_0} \\ \delta_{a1_0} \\ \delta_{a2_0} \\ \delta_{r1_0} \\ \delta_{r2_0} \\ \omega_{1_0} \\ \omega_{2_0} \\ \omega_{3_0} \\ \omega_{4_0} \\ \omega_{5_0} \\ \omega_{6_0} \\ \omega_{7_0} \\ \omega_{8_0} \end{bmatrix} = \begin{bmatrix} -3.53^\circ \\ -3.53^\circ \\ 12.80\ N \\ 0^\circ \\ 0^\circ \\ 0^\circ \\ 0^\circ \\ 0 \\ 0 \\ 0 \\ 0 \\ 0 \\ 0 \\ 0 \\ 0 \end{bmatrix} rps^2 \tag{27}$$

Table 1 presents the original physical parameters of the Aerosonde UAV, as provided in (Beard & McLain, 2012), along with additional parameters required for its modification into an octoplane configuration.

The linearised model exhibited minimal cross-coupling between the lateral and longitudinal state variables. As a result, the state variables were divided into longitudinal and lateral subsystems for control

design. Neglecting the cross-coupling terms:

$$x_{long}(t) = [\theta \quad \alpha \quad V_{tas} \quad q]^T \tag{28}$$

$$x_{lat}(t) = [\phi \quad \beta \quad r \quad p]^T \tag{29}$$

The control inputs for the longitudinal and lateral systems are defined as follows:

$$u_{\text{long}}(t) = \left[\delta_{1_e} \quad \delta_{2_e} \quad \delta_T \quad \Omega_{1_{\text{long}}} \quad \Omega_{2_{\text{long}}} \quad \Omega_{3_{\text{long}}} \quad \Omega_{4_{\text{long}}} \quad \Omega_{5_{\text{long}}} \quad \Omega_{6_{\text{long}}} \quad \Omega_{7_{\text{long}}} \quad \Omega_{8_{\text{long}}}\right]^T \tag{30}$$

$$u_{\text{lat}}(t) = [\delta_{1_a} \quad \delta_{2_a} \quad \delta_{1_r} \quad \delta_{2_r} \quad \Omega_{1_{\text{lat}}} \quad \Omega_{2_{\text{lat}}} \quad \Omega_{3_{\text{lat}}} \quad \Omega_{4_{\text{lat}}} \quad \Omega_{5_{\text{lat}}} \quad \Omega_{6_{\text{lat}}} \quad \Omega_{7_{\text{lat}}} \quad \Omega_{8_{\text{lat}}}]^T \tag{31}$$

which correspond to the longitudinal inputs: left and right elevator deflections ($\delta_{1_e}, \delta_{2_e}$) (rad), engine thrust ($\delta_T$) (N), and the squared speeds of the eight vertical rotors ($\Omega_{i_{\text{long}}}$) (rps² or rad²/s²); and the lateral inputs: left and right aileron deflections ($\delta_{1_a}, \delta_{2_a}$) (rad), left and right rudder deflections ($\delta_{1_r}, \delta_{2_r}$) (rad), along with the squared speeds of the eight vertical rotors ($\Omega_{i_{\text{lat}}}$) (rps²).

**Table 1**

*The physical parameters of the octoplane*

| Original Param. | Value | Additional Param. | Value |
|---|---|---|---|
| $m$ | 13.5 kg | $C_{Mq}$ | $7.5 \times 10^{-7}$ N·m·s² |
| $J_x$ | 0.8244 kg·m² | $C_{Tq}$ | $3.13 \times 10^{-5}$ N·s² |
| $J_y$ | 1.135 kg·m² | $L_{arm1}$ | 1 m |
| $J_z$ | 1.759 kg·m² | $L_{arm2}$ | 1.5811 m |
| $J_{xz}$ | 0.1204 kg·m² | $\eta_1$ | 45° |
| $S_{aero}$ | 0.55 m² | $\eta_2$ | 63.4349° |
| $b$ | 2.8956 m | $\kappa$ | 1° |
| $c$ | 0.18994 m | $d$ | 0.3226 m |
| $S_{prop}$ | 0.2027 m² | $J_r$ | $6.0 \times 10^{-5}$ kg·m² |
| $\rho_{air}$ | 1.2682 kg/m³ | | |

**Sliding Mode Control Analysis**

In the presence of an actuator fault or failure, the linear systems representing the longitudinal and lateral dynamics can be expressed as (Alwi & Edwards, 2008):

$$\dot{x}(t) = Ax(t) + Bu(t) - BKu(t) \tag{32}$$

where $K = diag(k_1, \ldots, k_{\text{m}})$ is the fault matrix, and each $k_i$ satisfies $0 \leq k_{\text{i}} \leq 1$. Specifically, when $k_{\text{i}} = 0$, the $i$-th actuator is fault-free. On the other hand, if this actuator is subject to a total failure, $k_{\text{i}} = 1$, and $0 < k_{\text{i}} < 1$ corresponds to a partial fault. Following (Alwi & Edwards, 2008), it is assumed that the values of $k_{\text{i}}$ are known (either through a fault detection and isolation (FDI) system or through actuator deflection measurements compared to the demand signal. These measurements are commonly available in aircraft systems). Using this fault information, control inputs can be reallocated among healthy actuators. For this purpose, the actuator effectiveness matrix is defined as $W = diag(w_1, \ldots, w_{\text{m}})$ where

$$W = I_{\text{m}} - K \tag{33}$$

and $I_{\text{m}}$ is the identity matrix. Based on the control allocation framework in (Alwi & Edwards, 2010), the input matrix $B$ in (32) can be partitioned as:

$$B = \begin{bmatrix} B_1 \\ B_2 \end{bmatrix} \tag{34}$$

where $B_1 \in \mathbb{R}^{(n-l)xm}$ and $B_2 \in \mathbb{R}^{lxm}$, with $rank(B_2) = l < m$.

As discussed in (Alwi & Edwards, 2010), $B_2$ represents the dominant effect of the control inputs. In contrast, $B_1$ contains relatively small terms compared to $B_2$. Unlike many studies that assume $B_1 = 0$, this study considers $B_1 \neq 0$. It is also assumed that state variables in (32) have been transformed such that $B_2 B_2^{\mathrm{T}} = I_2$.

For CA analysis, define the 'virtual control signal' as

$$v(t) = B_2 u(t) \tag{35}$$

where $u(t)$ is

$$u(t) = B_2^{\dagger} v(t) \tag{36}$$

Here $B_2^{\dagger}$ is a right pseudo-inverse of $B_2$, and is given by

$$B_2^{\dagger} = W B_2^{\mathrm{T}} (B_2 W B_2^{\mathrm{T}})^{-1} \tag{37}$$

So that $B_2 B_2^{\dagger} = I_l$.

Using (36) in (32) yields

$$\dot{x}(t) = Ax(t) + \underbrace{\begin{bmatrix} B_1 B_2^{\dagger} \\ I_l \end{bmatrix}}_{B_v} v(t) - \begin{bmatrix} B_1 K B_2^{\dagger} \\ B_2 K B_2^{\dagger} \end{bmatrix} v(t) \tag{38}$$

The objective is to design a virtual control $v(t)$ (of lower order than $u(t)$) using SMC as proposed in (Edwards & Spurgeon, 1998).

Here, the switching function is defined as $s(t) = Sx(t)$, and the sliding surface is

$$\boldsymbol{S} = \{x(t) \in \mathbb{R}^n : Sx(t) = 0\} \tag{39}$$

where $S \in \mathbb{R}^{l \times n}$ and $det(SB_v) \neq 0$. Since $K = I - W$ the system in (38) can be written as

$$\dot{x}(t) = Ax(t) + \begin{bmatrix} B_1 W^2 B_2^T (B_2 W B_2^T)^{-1} \\ B_2 W^2 B_2^T (B_2 W B_2^T)^{-1} \end{bmatrix} v(t) \tag{40}$$

Let $\bar{v}(t) = (B_2 W B_2^T)^{-1} v(t)$, then (40) can be written as

$$\dot{x} = Ax(t) + \begin{bmatrix} B_1 B_2^T \\ I \end{bmatrix} \bar{v}(t) - \begin{bmatrix} B_1 (I - W^2) B_2^T \\ B_2 (I - W^2) B_2^T \end{bmatrix} \bar{v} \tag{41}$$

The following coordinate transformation (Edwards & Spurgeon, 1998) is applied to express the system (41) in 'regular form'

$$x(t) \to T_r x(t) = \hat{x} \tag{42}$$

where

$$T_r = \begin{bmatrix} I & -B_1 B_2^T \\ 0 & I \end{bmatrix} \tag{43}$$

Substituting (42) and (43) into (41) yields

$$\dot{\hat{x}}(t) = \hat{A}\hat{x}(t) + \begin{bmatrix} 0 \\ I \end{bmatrix} \bar{v}(t) - \begin{bmatrix} B_1 B_2^N (I - W^2) B_2^T \\ B_2 (I - W^2) B_2^T \end{bmatrix} \bar{v}(t) \tag{44}$$

where $\hat{A} = T_r A T_r^{-1}$ and define $B_2^N = (I - B_2^T B_2)$. Since $B_2 B_2^T = I_l$ and $B_2^N B_2^T = (I - B_2^T B_2) B_2^T = 0$, therefore

$$B_1 B_2^N (I - W^2) B_2^T = -B_1 B_2^N W^2 B_2^T \tag{45}$$

Hence, (44) simplifies to:

$$\dot{\hat{x}}(t) = \hat{A}\hat{x}(t) + \begin{bmatrix} 0 \\ B_2 W^2 B_2^T \end{bmatrix} \bar{v}(t) - \begin{bmatrix} B_1 B_2^N W^2 B_2^T \\ 0 \end{bmatrix} \bar{v}(t) \tag{46}$$

The last term in (46) becomes zero in the case of fault-free. On the other hand, this term is considered as the unmatched uncertainty when $W \neq I$.

Define an alternative nonsingular scaling of the virtual control signal as

$$\hat{v}(t) = (B_2 W^2 B_2^T)\bar{v}(t) \tag{47}$$

Therefore, (46) can be rewritten as

$$\begin{bmatrix} \dot{\hat{x}}_1(t) \\ \dot{\hat{x}}_2(t) \end{bmatrix} = \begin{bmatrix} \hat{A}_{11} & \hat{A}_{12} \\ \hat{A}_{21} & \hat{A}_{22} \end{bmatrix} \begin{bmatrix} \hat{x}_1(t) \\ \hat{x}_1(t) \end{bmatrix} + \begin{bmatrix} 0 \\ I \end{bmatrix} \hat{v}(t) + \begin{bmatrix} B_1 B_2^N B_2^* \\ 0 \end{bmatrix} \hat{v}(t) \tag{48}$$

where $B_2^* = W^2 B_2^T (B_2 W^2 B_2^T)^{-1}$

***Proposition 1:***

There exists a finite constant $\gamma_0$, independent of $W$, for which

$$||B_2^*|| = ||W^2 B_2^T (B_2 W^2 B_2^T)^{-1}|| < \gamma_0 \tag{49}$$

holds for all $0 < w_i < 1$, provided that $\det(B_2 W^2 B_2^T) \neq 0$

***Proof 1:*** A similar argument to that in *(Alwi & Edwards, 2008)*. ■

Since $B_1 B_2^N B_2^* = 0$ in the absence of faults, the virtual control input $\hat{v}(t)$ can be formulated based on the nominal (fault-free) system, where the last term in (48) vanishes. An appropriate choice for the switching surface in (49) is given by

$$\hat{S} = S T_r^{-1} = [M \quad I_l] \tag{50}$$

where $M \in \mathbb{R}^{l \times (n-l)}$ denotes a design parameter.

Subsequently, a new coordinate transformation is introduced such that $(\hat{x}_1, \hat{x}_2) \rightarrow (\hat{x}_1, s)$, where

$$T_{r^*} = \begin{bmatrix} I & 0 \\ M & I \end{bmatrix} \tag{51}$$

Under this transformation, (48) can be rewritten as

$$\begin{bmatrix} \dot{\hat{x}}_1(t) \\ \dot{s}(t) \end{bmatrix} = \begin{bmatrix} \bar{A}_{11} & \bar{A}_{12} \\ \bar{A}_{21} & \bar{A}_{22} \end{bmatrix} \begin{bmatrix} \hat{x}_1(t) \\ s(t) \end{bmatrix} + \begin{bmatrix} B_1 B_2^N B_2^* \\ I + M B_1 B_2^N B_2^* \end{bmatrix} \hat{v}(t) \tag{52}$$

where

$$\bar{A}_{11} = \hat{A}_{11} - \hat{A}_{12} M \tag{53}$$

and

$$\bar{A}_{21} = M\bar{A}_{11} + \hat{A}_{21} - \hat{A}_{22} M \tag{54}$$

During an ideal sliding motion, $\dot{s}(t) = s(t) = 0$, and the equivalent control input $\hat{v}_{eq}$ required to maintain this sliding condition can be derived from the second row of (52), which is given by

$$\hat{v}_{eq}(t) = -(I + M B_1 B_2^N B_2^*)^{-1} \bar{A}_{21} \hat{x}_1(t) \tag{55}$$

Define the scalar

$$\gamma_1 = ||M B_1 B_2^N|| \tag{56}$$

the following inequality can be derived by combining (49) and (56)

$$||M B_1 B_2^N B_2^*|| < ||M B_1 B_2^N|| \, ||B_2^*|| < \gamma_0 \gamma_1 \tag{57}$$

If the pair $(A, B_v)$ is controllable, then the transformed pair $(\hat{A}_{11}, \hat{A}_{12})$ will also remain controllable (Edwards & Spurgeon, 1998). Therefore, this controllability condition enables the selection of $M$ such that the matrix $\hat{A}_{11} - \hat{A}_{12}M$ is stable. Furthermore, if $M$ is selected to ensure that $\gamma_1$, as defined in (56), satisfies the condition $\gamma_0\gamma_1 < 1$, this guarantees the inverse in (55) is well defined for all $W$.

Substituting (55) into the upper block of (52) yields the reduced-order system that governs the sliding dynamics.

$$\dot{\hat{x}}_1(t) = \bar{A}_{11}\hat{x}_1(t) - B_1 B_2^N B_2^*(I + MB_1 B_2^N B_2^*)^{-1}\bar{A}_{21}\hat{x}_1(t) \tag{58}$$

In the fault-free case, $W = I$, which implies $B_2^* = B_2^T$, since $B_2 B_2^T = I$. Under this condition, the system simplifies as follows:

$$B_2^N B_2^* = (I - B_2^T B_2)B_2^* = (I - B_2^T B_2)B_2^T = 0 \tag{59}$$

and therefore, in the fault-free scenario, the reduced-order system described by (58) simplifies to:

$$\dot{\hat{x}}_1(t) = \bar{A}_{11}\hat{x}_1(t) \tag{60}$$

which represents the nominal fault-free sliding-mode reduced-order system, whose stability is ensured by the appropriate selection of the matrix $M$. In contrast, in the presence of faults or failures, $W \neq I$ and (58) depends on $W$. As a result, stability needs to be established under fault or failure conditions.

***Stability Analysis***

The stability of the sliding mode is determined by the reduced-order system in (58). This stability primarily depends on the matrix $\bar{A}_{11}$, which is ensured by designing the matrix $M$ through standard hyperplane design techniques, under the assumption of a nominal fault-free condition where $W = I$. To evaluate stability under fault or failure conditions (i.e., when $W \neq I$), the small gain theorem (Alwi & Edwards, 2008) is employed. For this purpose, the following transfer function is defined as

$$\bar{G}(\mathbf{s}) = \bar{A}_{21}(sI - \bar{A}_{11})^{-1}B_1 B_2^N \tag{61}$$

where $s$ denotes the Laplace variable, and $\bar{G}(\mathbf{s})$ is the transfer function matrix. Also, define

$$\gamma_2 = |\bar{G}(\mathbf{s})|_\infty \tag{62}$$

*Proposition 2*

The closed-loop system remains stable for any value of $0 < w_i \leq 1$ as long as the following condition holds

$$0 \leq \frac{\gamma_2\gamma_0}{1 - \gamma_1\gamma_0} < 1 \tag{63}$$

where the parameters $\gamma_0, \gamma_1, \gamma_2$ are represented by (49), (56) and (62), respectively.

*Proof 2:* This is similar to the one presented in *(Alwi & Edwards, 2008)*. ■

The coefficients $\gamma_1$and $\gamma_2$ depend on the matrix $M$, and therefore are affected by the design of the sliding surface. However, these coefficients are independent of $W$. In contrast, the scalar coefficient $\gamma_0$ is influenced by $W$, but not by $M$.

If $B_1 = 0$, both coefficients $\gamma_1$and $\gamma_2$ become zero, ensuring that (63) is satisfied. Moreover, as $||B_1|| \to 0$, the scalar term $\frac{\gamma_2\gamma_0}{1-\gamma_1\gamma_0}$ approaches zero. Therefore, (63) provides a stability check for the closed-loop system in the presence of faults or failures.

***Sliding Mode Control Methods***

As previously mentioned, the virtual control $\hat{v}(t)$ in (48) is designed under the assumption of a fault-free case ($W = I$). The control law comprises linear and nonlinear parts, represented as follows:

$$\hat{v}(t) = \hat{v}_l(t) + \hat{v}_n(t) \tag{64}$$

where the linear part $\hat{v}_l(t)$ is given by

$$\hat{v}_l(t) = -\hat{A}_{21}\hat{x}_1(t) - \hat{A}_{22}s(t) \tag{65}$$

and the nonlinear part $\hat{v}_n(t)$ is defined as

$$\hat{v}_n(t) = -K(t,x)\frac{s(t)}{||s(t)||} \quad if s(t) \neq 0 \tag{66}$$

*Proposition 3*

If the design matrix $M$ is selected such that $\bar{A}_{11} = \hat{A}_{11} - \hat{A}_{12}M$ is stable and satisfies the condition in (63), then the following choice of gain ensures that the sliding motion reaches the surface $\boldsymbol{S}$ in finite time:

$$K = \frac{\gamma_1\gamma_0||\hat{v}_l(t)|| + \eta}{1 - \gamma_1\gamma_0} \tag{67}$$

*Proof 3:* A similar approach to *(Alwi & Edwards, 2008)* can be used here. ■

The actual control input sent to the actuators is determined by employing $\hat{v}(t)$ from (64)-(66), and using (36), (37) and (47), and $u(t)$ can be written as

$$u(t) = WB_2^T(B_2W^2B_2^T)^{-1}\hat{v}(t) \tag{68}$$

The term $WB_2^T(B_2W^2B_2^T)^{-1}$ in (68) is commonly known as the CA matrix. This matrix distributes the control signals among all actuators and is directly influenced by the actuator effectiveness matrix $W$.

**Design of Controller for Tracking Requirement**

Integral action is included to allow tracking of four controlled state variables: true airspeed ($V_{tas}$) and flight path angle ($\gamma = \theta - \alpha$) by the longitudinal controller, and roll angle ($\phi$) and sideslip angle ($\beta$) by the lateral controller. The overall structure of the online control allocation (CA) scheme is illustrated in Figure 5. It is assumed that the actuator effectiveness levels are known and provided by the fault detection and isolation (FDI) unit.

A new state variable $x_r(t) \in \mathbb{R}^l$ is defined as

$$\dot{x}_{rc}(t) = r_c(t) - C_c x(t) \tag{69}$$

where $C_c$ is the output matrix that selects the controller state variables and $r_c(t)$ is the filtered demand signal, and is given by

$$\dot{r}(t) = \Gamma_c\big(r_c(t) - R(t)\big) \tag{70}$$

Here, $\Gamma_c$ is a stable design matrix, and $R(t)$ denotes a constant desired reference. Separate $C_c$ matrices are used for the longitudinal and lateral controllers, and are given by

$$C_{c_{long}} = \begin{bmatrix} 0 & 0 & 1 & 0 \\ 1 & -1 & 0 & 0 \end{bmatrix}, C_{c_{lat}} = \begin{bmatrix} 1 & 0 & 0 & 0 \\ 0 & 1 & 0 & 0 \end{bmatrix} \tag{71}$$

The system state is then augmented with the new state variables to yield

$$x_a(t) = \begin{bmatrix} x_r(t) \\ x(t) \end{bmatrix} \tag{72}$$

The system in (32) is transformed into the augmented form and becomes

$$\dot{x}_a(t) = A_a x_a(t) + B_a v(t) + B_r r_c(t) \tag{73}$$

where the system matrices are defined as

$$A_a = \begin{bmatrix} 0 & -C_c \\ 0 & A \end{bmatrix}, \; B_a = \begin{bmatrix} 0 \\ B_v \end{bmatrix}, \; B_r = \begin{bmatrix} I \\ 0 \end{bmatrix} \tag{74}$$

The controller aims to induce and maintain a sliding motion along the defined surface

$$\boldsymbol{S}_a = \{x_a \in \mathbb{R}^{n+m} : S_a x_a = 0\} \tag{75}$$

where $S_a \in \mathbb{R}^{l\times(l+n)}$, and the augmented switching function is given by

$$s_a(t) = S_a x_a(t) = [M_a \quad I] x_a(t) \tag{76}$$

and $M_a \in \mathbb{R}^{n\times l}$. The augmented state variables can be partitioned into two components such that

$$x_a(t) = \begin{bmatrix} x_1(t) \\ x_2(t) \end{bmatrix} \tag{77}$$

where $x_1(t) \in \mathbb{R}^n, x_2(t) \in \mathbb{R}^l$. The matrix $A_a$ can be divided into four parts, and represented by

$$A_a = \begin{bmatrix} A_{a_{11}} & A_{a_{12}} \\ A_{a_{21}} & A_{a_{22}} \end{bmatrix} \tag{78}$$

Assuming the controller successfully achieves ideal sliding motion on the designated hyperplane, the resulting reduced-order dynamics can be expressed as

$$\dot{x}_1(t) = \left(A_{a_{11}} - A_{a_{12}} M_a\right) x_1(t) + \bar{B}_r r_c(t) \tag{79}$$

where $\bar{B}_r$ is the top $n$ rows of $B_r$ from (74). From (79), the controllability of the matrices $A_{a_{11}}$ and $A_{a_{12}}$ is essential for a stable motion on the sliding surface. According to (Edwards & Spurgeon, 1998), this condition is satisfied if the overall pair $(A_a, B_a)$ is controllable, which is guaranteed and provided the triple $(A, B, C)$ has no invariant zeros at the origin (Alwi & Edwards, 2008).

As previously discussed, the proposed controller for the augmented system is composed of two parts:

$$\hat{v}(t) = \hat{v}_l(t) + \hat{v}_n(t) \tag{80}$$

The discontinuous part is defined as

$$\hat{v}_n(t) = \begin{cases} K \dfrac{\bar{P}_2 s}{||\bar{P}_2 s||} & \text{if } s_a \neq 0 \\ 0 & \text{otherwise} \end{cases} \tag{81}$$

and, $\bar{P}_2$ denotes a symmetric positive definite matrix that satisfies the Lyapunov equation

$$\bar{P}_2 \Phi + \Phi^T \bar{P}_2 = -I \tag{82}$$

where $\Phi \in \mathbb{R}^{m\times m}$ represents a stable design matrix.

Note that compared to (66), the terms $\bar{P}_2$ (and therefore $\Phi$ in (88)) have been included in (81) for practical implementation. As discussed in (Alwi et al., 2011; Edwards & Spurgeon, 1998), the term $\Phi$ accelerates the sliding motion relative to the original formulation in (66).

The linear part of the controller $\hat{v}_l(t)$ in (80) is defined as

$$\hat{v}_l(t) = L x_a(t) + L_r r_c(t) \tag{83}$$

where $L$ and $L_r$ are the feedback gains (Edwards & Spurgeon, 1998), and are given by

$$L = -(S_a A_a - \Phi S_a), \qquad L_r = -M_a B_r \tag{84}$$

In this paper, the matrix $S_a$ is determined using a quadratic minimisation approach (Edwards & Spurgeon, 1998; V. I. Utkin, 1979). The symmetric positive definite weighting matrices have been selected as

$$Q_{long} = diag(1, 5, 10, 10, 1, 2) \tag{85}$$

$$Q_{lat} = diag(1,1,1,1,1,1) \tag{86}$$

and the stable design matrices are selected as

$$\Phi_{long} = diag(-2, -2) \tag{87}$$

$$\Phi_{lat} = diag(-2, -2) \tag{88}$$

The poles of the reduced-order sliding motion for both the longitudinal and lateral controllers are as follows:

$$E_{long} = (-0.8474,\ -1.0002, -1.3556,\ -3.9481) \tag{89}$$

$$E_{lat} = (-0.7296, -0.8849 \pm 0.5010i, -1.2953) \tag{90}$$

The filter parameters have been specified as

$$\Gamma_{long} = -2.5I_2,\ \Gamma_{lat} = -2.5I_2 \tag{91}$$

The nonlinear modulation gains are set to

$$K_{long} = 5I_2,\ K_{lat} = I_2 \tag{92}$$

respectively.

Finally, a sigmoidal approximation (Alwi et al., 2011) has been implemented to smooth the discontinuity in (81) so that

$$\frac{\bar{P}_2 s}{||\bar{P}_2 s|| + \delta_a} \tag{93}$$

where $\delta_a = 0.01$, $\bar{P}_2 = I_2$ have been selected for both the longitudinal and lateral controllers.

**Figure 5**

*The general controller diagram of the aircraft*

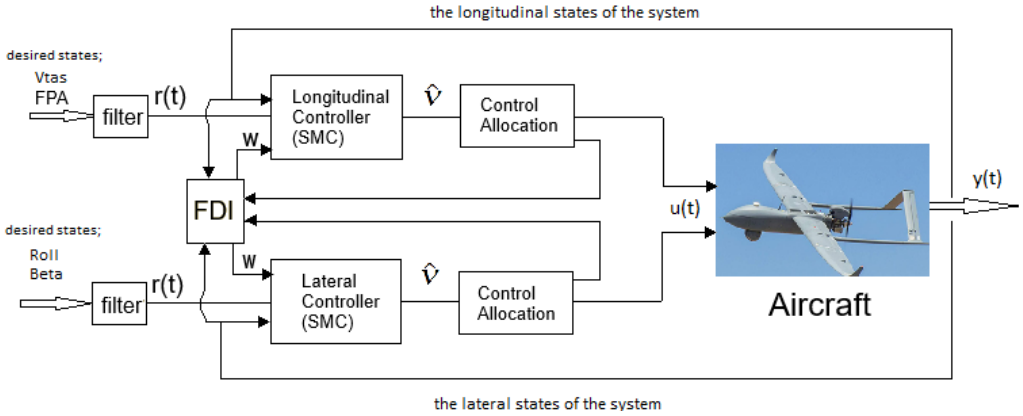


***Stability Analysis for Design***

The norms of $B_1$ and $B_2$ matrices (the partition of $B$ matrices, as discussed in (34)) for the longitudinal and lateral axes are given by

$$||B_{2_{long}}|| = 1, ||B_{2_{lat}}|| = 1, ||B_{1_{long}}|| = 0.1946, ||B_{1_{lat}}|| = 0.0919 \tag{94}$$

As seen in (94), $B_2$ matrices for both the lateral and longitudinal axes have a significantly greater influence on the control input compared to $B_1$.

The controller is designed based on the fault-free case in (48). To guarantee its stability under fault or failure conditions, a stability analysis is performed to ensure that conditions (49) and (63) are satisfied. First, $\gamma_0$ from (49) needs to be computed for all potential fault or failure cases. It is considered that there are no redundant actuators for controlling $V_{tas}$, and the propeller is assumed to be failure-free (e.g. $0 < \omega_{\delta_T} \leq 1$). Additional redundancies exist from the control surfaces (ailerons, elevators, rudders) and the eight vertical rotors for controlling flight path angle (FPA), roll, and sideslip. For FPA control, either the elevators alone or two vertical rotors (one front, one rear) suffice in fault/failure scenarios. In case of a forward propeller failure, the aircraft can temporarily maintain controlled flight by pitching nose-down and using gravity to achieve an airspeed of approximately 10 m/s. However, this study focuses specifically on steady-state cruise conditions at speeds exceeding 30 m/s, where gravity-assisted compensation alone would be insufficient. For roll control, either the ailerons or two of the vertical rotors (one from the left side and one from the right) are adequate to provide the desired motion about the roll axis. For sideslip control, either the rudders or two of the vertical rotors (one clockwise and one counterclockwise) are sufficient to maintain directional stability.

Under the stated assumptions, it can be established that $\det(B_2 W B_2^T) \neq 0$ for both axes and therefore $B_2 W B_2^T$ retains full rank. A numerical search yields

$$\gamma_{0_{long}} = 1.4142, \text{ and } \gamma_{0_{lat}} = 1.4142 \tag{95}$$

Using (56) yields

$$\gamma_{1_{long}} = 1.6712 \times 10^{-7}, and \gamma_{1_{lat}} = 2.9875 \times 10^{-9} \tag{96}$$

and therefore,

$$\gamma_{0_{long}}\gamma_{1_{long}} = 2.3634 \times 10^{-7} < 1, and \gamma_{0_{lat}}\gamma_{1_{lat}} = 2.9875 \times 10^{-9} < 1 \tag{97}$$

These results indicate that the requirements of *Proposition 2* are satisfied. Furthermore, for the chosen sliding surface, analysis reveals that

$$||\bar{G}_{long}(s)|| < \gamma_{2_{long}} = 0.2084 \times 10^{-5} \tag{98}$$

and

$$||\bar{G}_{lat}(s)|| < \gamma_{2_{lat}} = 2.3188 \times 10^{-7} \tag{99}$$

Therefore, from (63)

$$\frac{\gamma_{2_{long}}\gamma_{0_{long}}}{1 - \gamma_{1_{long}}\gamma_{0_{long}}} < 2.9484 \times 10^{-5} < 1 \tag{100}$$

and

$$\frac{\gamma_{2_{lat}}\gamma_{0_{lat}}}{1 - \gamma_{1_{lat}}\gamma_{0_{lat}}} < 3.2792 \times 10^{-7} < 1 \tag{101}$$

which confirms that the closed-loop systems remain stable under all potential actuator fault or failure scenarios.

**Results**

The results in this section are based on the nonlinear model (1-10) implemented in SIMULINK using the ODE14X solver with a step size of 0.01 seconds. To evaluate the effectiveness of the proposed method, four scenarios were tested, including one fault-free case and three fault/failure cases, as outlined

in Table 2 and Table 3. This paper focuses on cruise mode and evaluates performance in terms of desired lateral and longitudinal tracking. Identical manoeuvres are executed across all scenarios to provide comparison. In fault-free conditions, control is primarily achieved using standard control surfaces (aileron, elevator, rudder). In fault/failure cases (test cases 2–4), vertical rotors, typically used for VTOL, are utilised to maintain tracking performance as shown in the fault-free case. The simulation results show that the proposed scheme maintains tracking performance within ±1% error under the fault-free case. Even in fault and failure cases, the method achieves more than 95% tracking performance, exhibiting only minor degradation compared to the nominal case. In addition, the coupling effects between longitudinal and lateral states (e.g., roll and flight path angle) are negligible.

***Fault-free Scenario***

Figure 6-7 indicates the results under nominal conditions with all actuators functioning. Figures 6a-b demonstrate good tracking performance for longitudinal and lateral states. The simulation begins with a 25° roll manoeuvre lasting 20 seconds, maintaining near-zero sideslip, followed by a 3 m/s change in $V_{tas}$ at 40 seconds and a 12.5° FPA change from 70 to 90 seconds. Figure 6b reveals minor roll-sideslip coupling. As shown in Figure 7, the control surfaces are more active than the vertical rotors during nominal flight.

**Table 2**
Test cases: control surface effectiveness levels $w_i$

| No | Cases | $\delta_{e_1}$ | $\delta_{e_2}$ | $\delta_T$ | $\delta_{a_1}$ | $\delta_{a_2}$ | $\delta_{r_1}$ | $\delta_{r_2}$ |
|---|---|---|---|---|---|---|---|---|
| 1 | Fault-free | 1 | 1 | 1 | 1 | 1 | 1 | 1 |
| 2 | Faults/failures | 0.5 | 0 | 1 | 0.5 | 0 | 0.5 | 0 |
| 3 | Only elevator fails | 0 | 0 | 1 | 1 | 1 | 1 | 1 |
| 4 | Aileron and Rudder fail | 1 | 1 | 1 | 0 | 0 | 0 | 0 |

**Table 3**
Test cases: vertical rotors effectiveness levels $w_i$

| No | Cases | $\Omega_1$ | $\Omega_2$ | $\Omega_3$ | $\Omega_4$ | $\Omega_5$ | $\Omega_6$ | $\Omega_7$ | $\Omega_8$ |
|---|---|---|---|---|---|---|---|---|---|
| 1 | Fault-free | 1 | 1 | 1 | 1 | 1 | 1 | 1 | 1 |
| 2 | Faults/failures | 0 | 0.5 | 0.5 | 0.5 | 0.5 | 0.5 | 0 | 0.5 |
| 3 | Only elevator fails | 1 | 1 | 1 | 1 | 1 | 1 | 1 | 1 |
| 4 | Aileron and Rudder fail | 1 | 1 | 1 | 1 | 1 | 1 | 1 | 1 |

***Faults/failures scenario***

This scenario involves faults/failures across all control inputs, as detailed in Case 2 (Tables 2-3). One elevator, one aileron, one rudder, rotor 1, and rotor 7 have completely failed, while the remaining inputs operate at 50% effectiveness. The input signals are shown in Figure 9. Despite the faults and failures, Figures 8a-8b show minimal tracking degradation, and Figure 9b confirms that sliding remains near zero, demonstrating the robustness of the proposed scheme.

***Only the elevator fails***

This scenario refers to case 3 in Tables 2-3, where both elevators have failed while all other actuators remain healthy. As shown in Figures 10a and 10b, the demanded command can still be executed smoothly by reallocating control signals to the vertical rotors, as seen in Figure 11b. Figure 10c shows that the switching functions are close to zero, indicating a sliding motion is retained despite

the elevator failure.

### *Aileron and Rudder Fail*

This scenario, corresponding to case 4 in Tables 2-3, tests failures in the lateral control surfaces (ailerons and rudder). Despite these failures, Figures 12a and 12b show that good tracking performance is maintained employing the eight vertical rotors. As illustrated in Figure 13a, the aileron and rudder deflections are zero, and the control signals are effectively redistributed to the vertical rotors, which are more active than in the fault-free case. The switching function in Figure 13b remains close to zero, indicating that the sliding motion is maintained.

**Figure 6**

*Fault-free case – Longitudinal and lateral state variables and switching functions*

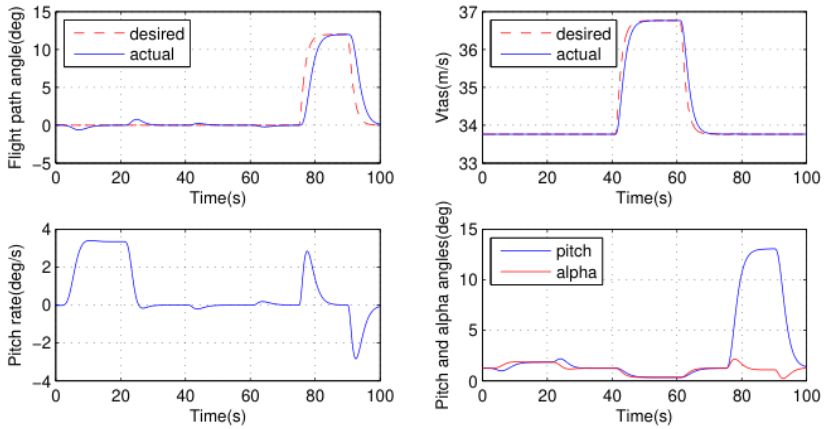


*Figure 6 a) Longitudinal state variables*

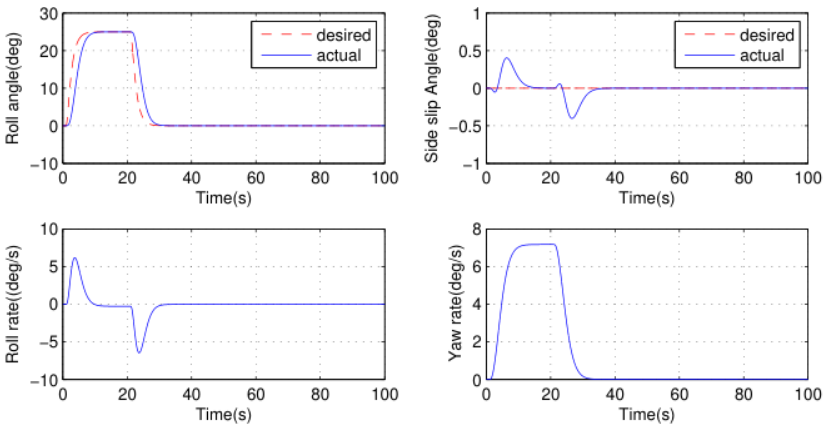


*Figure 6 b) Lateral state variables*

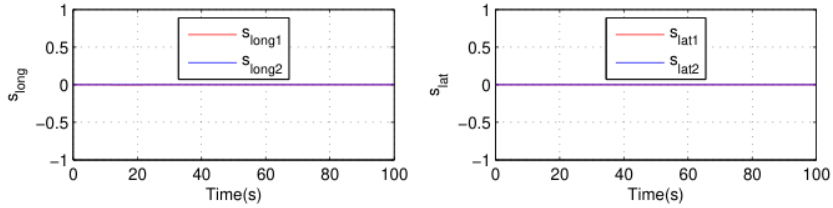


*Figure 6 c) Switching functions*

**Figure 7**
*Fault-free case – Control surfaces and vertical rotors*

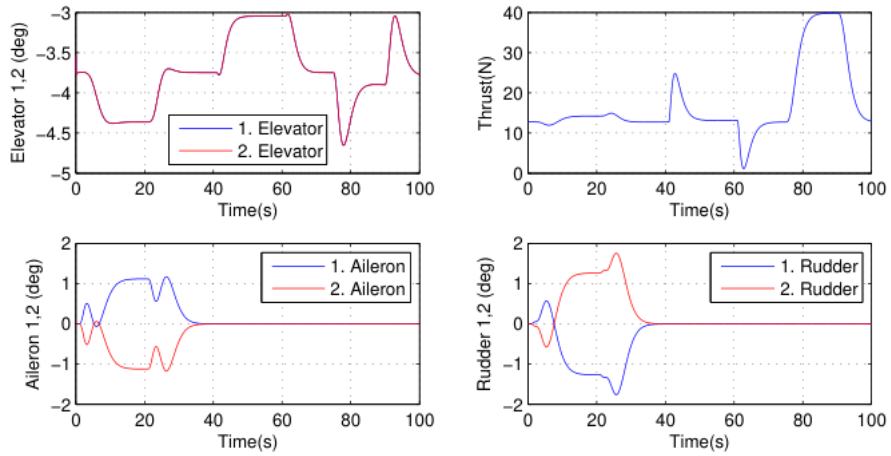


*Figure 7 a) Control surfaces*

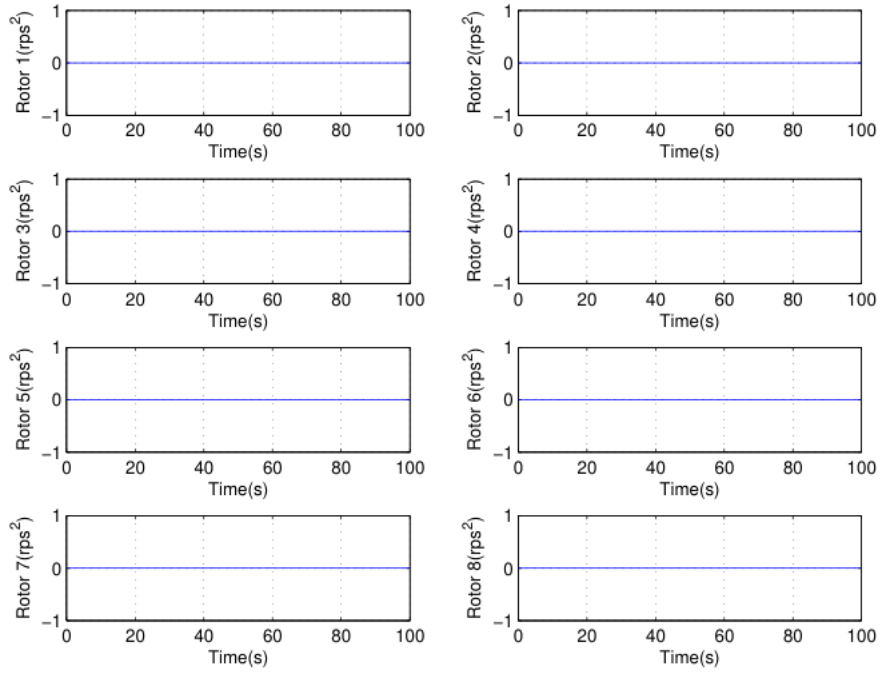


*Figure 7 b) Vertical rotors*

**Figure 8**

*Faults-failures case - Longitudinal and lateral state variables and switching functions*

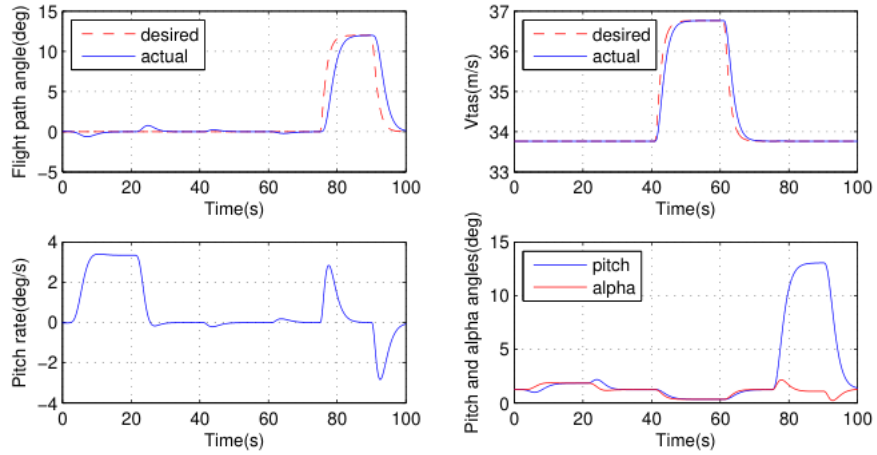


*Figure 8 a) - Longitudinal state variables*

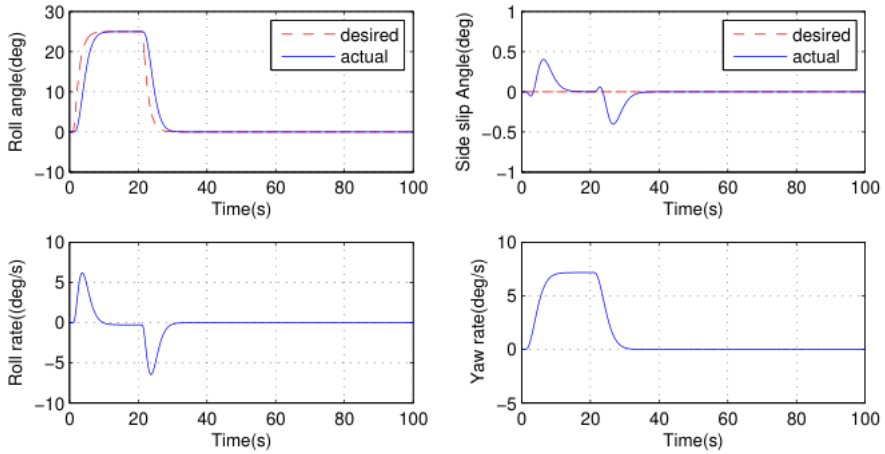


*Figure 8 b) Lateral state variables*

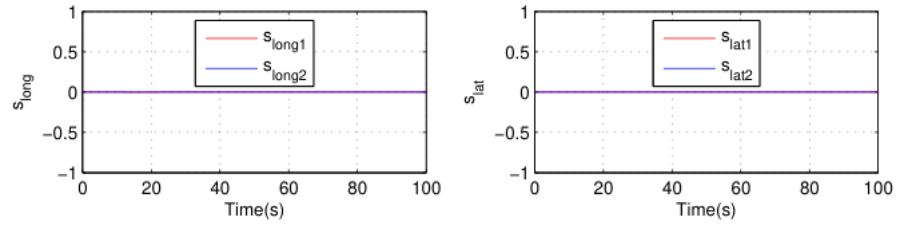


*Figure 8 c) Switching functions*

**Figure 9**
*Faults-failures case – Control surfaces and vertical rotors*

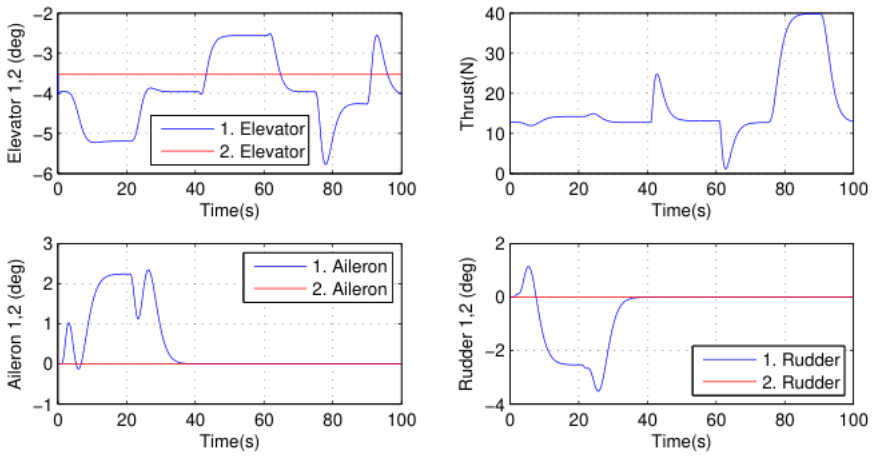


*Figure 9 a) Control surfaces*

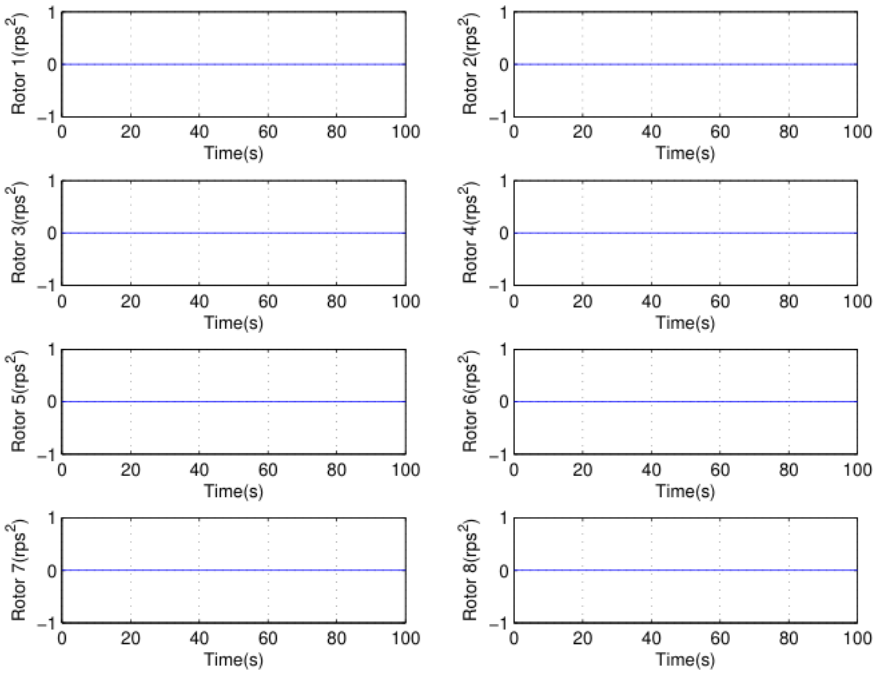


*Figure 9 b) Vertical rotors*

**Figure 10**
*Only elevator fails - Longitudinal and lateral state variables and switching functions.*

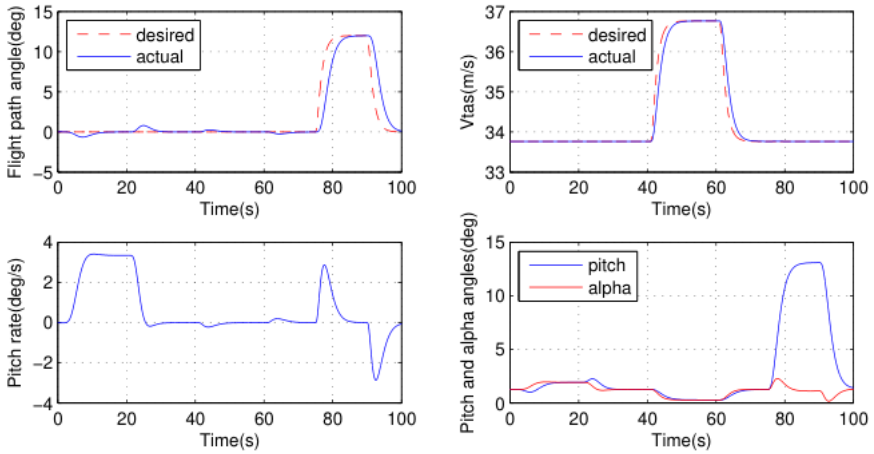


*Figure 10 a) Longitudinal state variables*

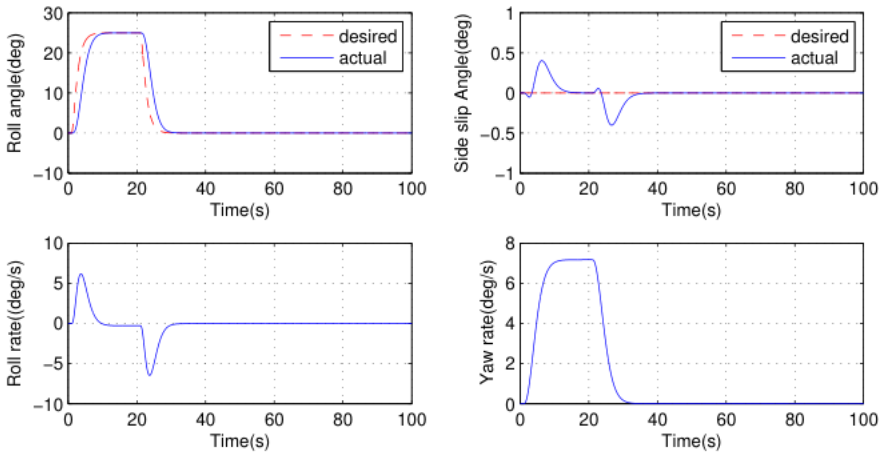


*Figure 10 b) Lateral state variables*

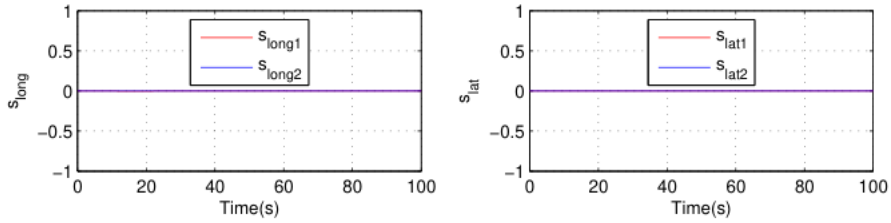


*Figure 10 c) Switching functions*

**Figure 11**
*Only elevator fails - Control surfaces and vertical rotors*

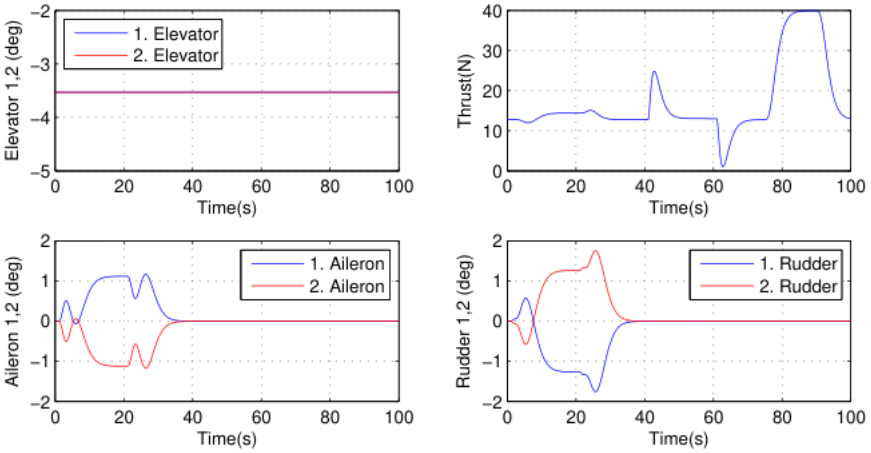


*Figure 11 a) Control surfaces*

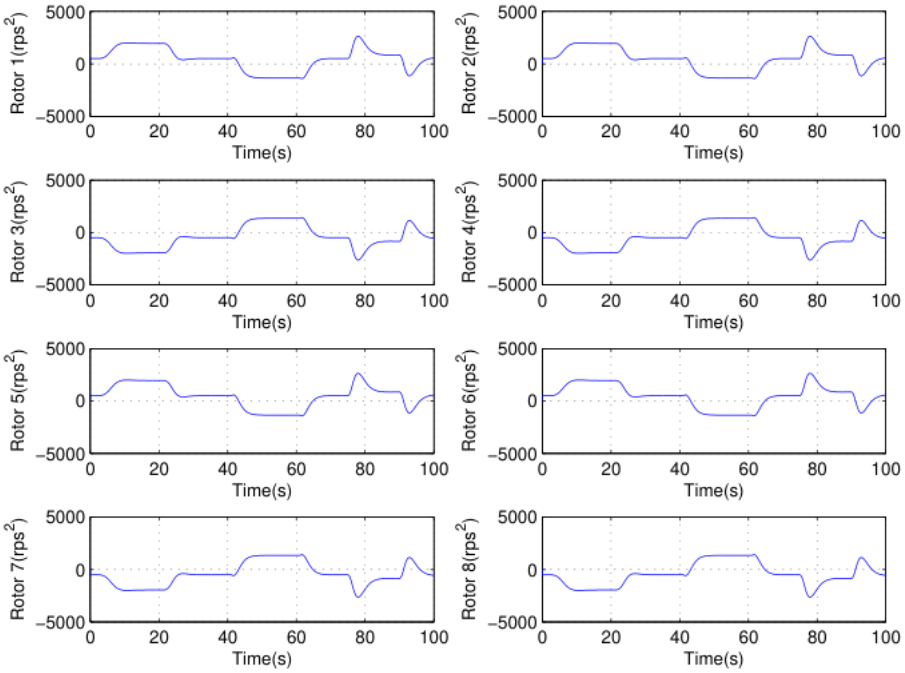


*Figure 11 b) Vertical rotors*

**Figure 12**

*Aileron and Rudder Fails - Longitudinal and lateral state variables and switching functions*

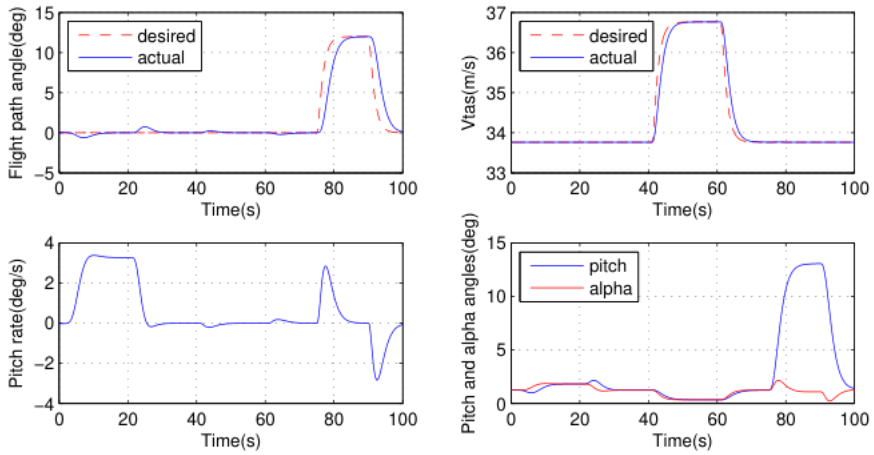


*Figure 12 a) Longitudinal state variables*

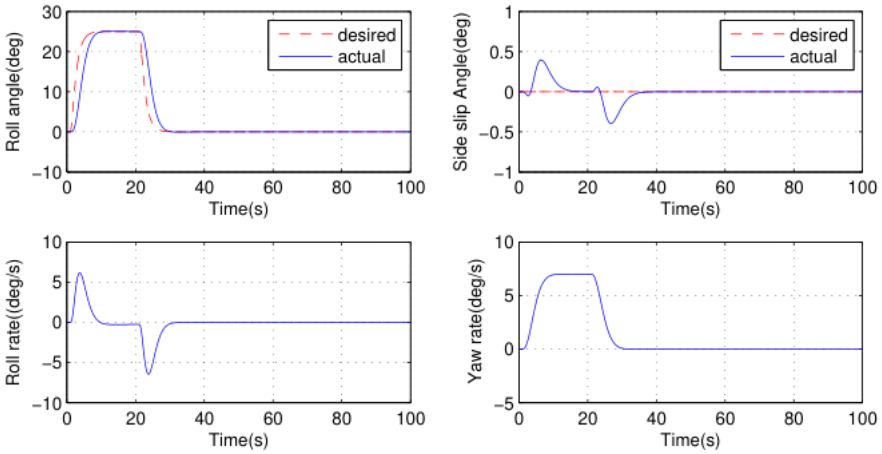


*Figure 12 b) Lateral state variables*

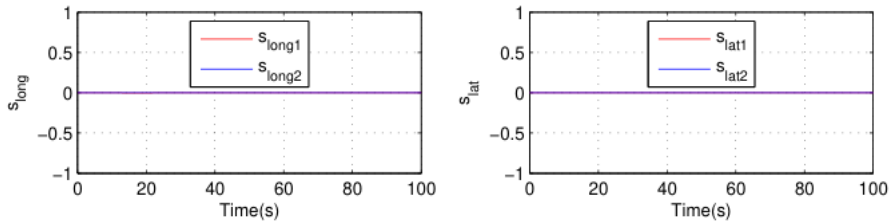


*Figure 12 c) Switching functions*

**Figure 13**

*Aileron and Rudder Fails - Control surfaces and vertical rotors*

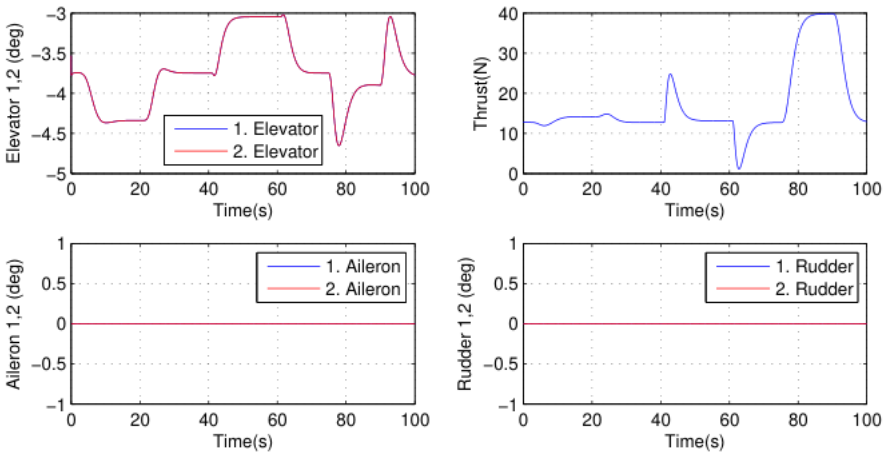


*Figure 13 a) Control surfaces*

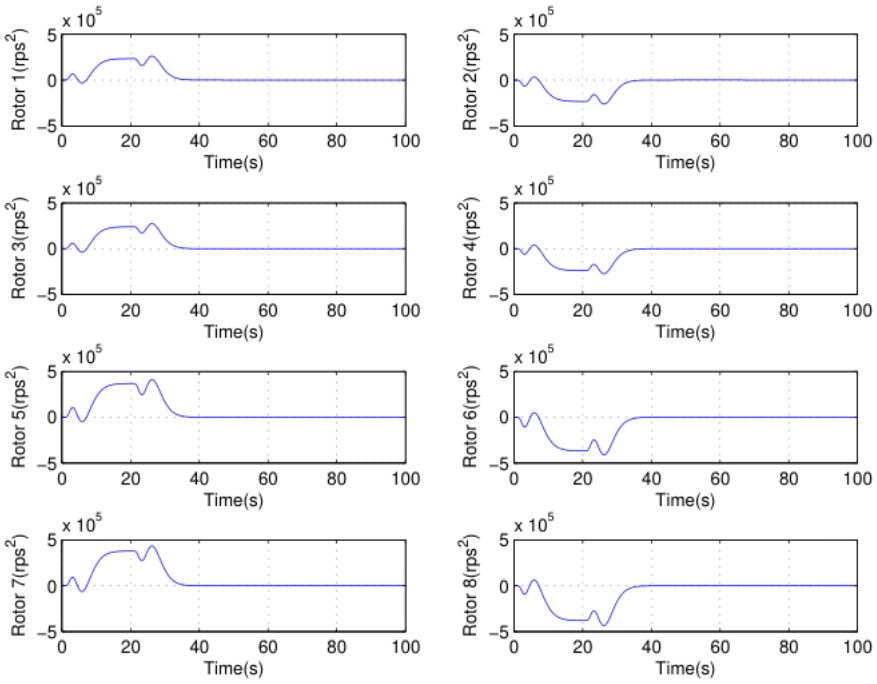


*Figure 13 b) Vertical rotors*

## Conclusion

This study proposes an SMC-based FTC scheme for an octoplane during cruise flight, exploiting the robustness of SMC and actuator redundancy from the control surfaces and eight vertical rotors. The CA redistributes control signals in the event of total actuator faults or failures, without requiring controller reconfiguration. Controllers are designed for both longitudinal (flight path angle and true airspeed) and lateral (roll and sideslip angles) dynamics. Four simulation scenarios, including fault-free and various failure/fault cases, show minimal tracking performance degradation, demonstrating the scheme's effectiveness.

## Ethical Statement

This study is derived from the doctoral thesis titled *"Fault Tolerant Control of Octoplane UAVs using Sliding Mode Control Techniques"*, submitted in 2024 under the supervision of Prof. Halim Alwi.

**Author Contributions**

Research Design (CRediT 1): Author 1 (60%) – Author 2 (20%) – Author 3 (20%)

Data Collection (CRediT 2): Author 1 (80%) – Author 2 (10%) – Author 3 (10%)

Research – Data Analysis – Validation (CRediT 3-4-6-11): Author 1 (70%) – Author 2 (15%) – Author 3 (15%)

Manuscript Writing (CRediT 12-13): Author 1 (80%) – Author 2 (10%) – Author 3 (10%)

Text Editing and Improvement (CRediT 14): Author 1 (70%) – Author 2 (15%) – Author 3 (15%)

**Funding**

This research was made possible by financial support from the Republic of Türkiye's Ministry of National Education Scholarship (MoNE-1416).

**REFERENCES**

Alwi, H., & Edwards, C. (2008). Fault tolerant control using sliding modes with on-line control allocation. *Automatica*, *44*(7), 1859–1866. https://doi.org/10.1016/j.automatica.2007.10.034

Alwi, H., & Edwards, C. (2010). Fault Tolerant Control Using Sliding Modes with On-Line Control Allocation. In C. Edwards, T. Lombaerts, & H. Smaili (Eds.), *Fault Tolerant Flight Control: A Benchmark Challenge* (pp. 247–272). Springer Berlin Heidelberg. https://doi.org/10.1007/978-3-642-11690-2_8

Alwi, H., Edwards, C., & Tan, C. P. (2011). *Fault Detection and Fault Tolerant Control Using Sliding Modes*. Springer-Verlag Berlin. https://doi.org/10.1007/978-0-85729-650-4

Anon. (2018). *Amrita Unmanned Aerial Systems*. https://ammachilabs.org/amrita-unmanned-aerial-systems/

Anon. (2019). *Saving Lives One Drone Delivery at a Time*. https://lot.dhl.com/saving-lives-one-drone-delivery-at-a-time

Anon. (2023). *Wing and FinnHEMS safely share the sky*. https://blog.wing.com/2023/07/wing-and-finnhems-safely-share-sky.html

Beard, R. W., & Mclain, T. W. (2012). *Small Unmanned Aircraft Theory and Practice*. Princeton Universty Press.

Bothge, L. (2022). *Meet the V.MO – Volkswagen Group China unveils state-of-the-art passenger drone prototype*. https://www.volkswagen-newsroom.com/en/press-releases/meet-the-vmo-volkswagen-group-china-unveils-state-of-the-art-passenger-drone-prototype-15116

Cai, J., & Lovera, M. (2024). Passive Fault Tolerant Control of a Dual-System UAV in Transition Flight. *ICAS PROCEEDINGS*, 1–14.

Dağ., T., Ünler, T., & Uyaner, M. (2023). Elektrikli İnsansız Hava Aracının Maksimum Menzil Hesabı. *Aerospace Research Letters (ASREL)*, *2*(1), 10–18.

Ducard, G. J. J., & Allenspach, M. (2021). Review of designs and flight control techniques of hybrid and convertible VTOL UAVs. *Aerospace Science and Technology*, *118*, 107035. https://doi.org/10.1016/j.ast.2021.107035

Edwards, C., & Spurgeon, S. (1998). *Sliding Mode Control*. CRC Press. https://doi.org/10.1201/9781498701822

Gu, H., Lyu, X., Li, Z., Shen, S., & Zhang, F. (2017). Development and experimental verification of a hybrid vertical take-off and landing (VTOL) unmanned aerial vehicle(UAV). *2017 International Conference on Unmanned Aircraft Systems (ICUAS)*, 160–169. https://doi.org/10.1109/ICUAS.2017.7991420

Heredia, G., Duran, A., & Ollero, A. (2012). Modeling and Simulation of the HADA Reconfigurable UAV. *Journal of Intelligent & Robotic Systems*, *65*, 115–122. https://doi.org/10.1007/s10846-011-9561-9

Honda Motor Co., Ltd. (2022). *eVTOL Gas Turbine Hybrid System*. https://global.honda/en/tech/eVTOL_gas_turbine_hybrid_system/

Ijaz, S., Javaid, U., Nasr, A., & Sun, D. (2024). Fault-Tolerant Control of Hybrid UAV Using Weighted Control Allocation Scheme. *2024 American Control Conference (ACC)*, 4687–4692. https://doi.org/10.23919/ACC60939.2024.10644250

Khattab, A., Mizrak, I., & Alwi, H. (2024). Fault tolerant control of an octorotor UAV using sliding mode for applications in challenging environments. *Annual Reviews in Control*, *57*, 100952. https://doi.org/10.1016/j.arcontrol.2024.100952

Köprücü, S., & Öztürk, M. (2024). Comparison of PID Coefficients Determination Methods for Aircraft Pitch Angle Control. *Aerospace Research Letters (ASREL)*, *3*(1), 15–26. https://doi.org/10.56753/ASREL.2024.3.5

Kringeland, T. (2019). *Modelling and Control of a Vertical Take-Off and Landing Fixed-Wing*

*Unmanned Aerial Vehicle* [Master's Thesis]. University Of Oslo.

Kulaksız, N., & Hançer, M. (2022). Hava Aracı için Simulink-FlightGear Ortamlarında Uçuş Testlerinin Gerçeklenmesi ve Aerodinamik Etkilerin Stabilite/Gövde Eksenlerinde Karşılaştırılması. *Aerospace Research Letters (ASREL)*, *1*(2), 69–83. https://dx.doi.org/10.56753/ASREL.2022.2.1

MathWorks. (2024). *MATLAB & SIMULINK User's Guide R2024b*.

Mizrak, I., Alwi, H., & Edwards, C. (2021). Fault Tolerant Control of an Octoplane UAV Using Sliding Modes. *5th International Conference on Control and Fault-Tolerant Systems (SysTol)*, 121–126. https://doi.org/10.1109/SysTol52990.2021.9595155

Mohsan, S. A. H., Khan, M. A., Noor, F., Ullah, I., & Alsharif, M. H. (2022). Towards the Unmanned Aerial Vehicles (UAVs): A Comprehensive Review. *Drones*, *6*(6). https://doi.org/10.3390/drones6060147

Munasinghe, R., & Gunarathna, J. (2018). Development of a Quad-rotor Fixed-wing Hybrid Unmanned Aerial Vehicle. *2018 Moratuwa Engineering Research Conference (MERCon)*, 72–77. https://doi.org/10.1109/MERCon.2018.8421941

Murphy, P. C., Buning, P. G., & Simmons, B. M. (n.d.). Rapid Aero Modeling for Urban Air Mobility Aircraft in Computational Experiments. In *AIAA Scitech 2021 Forum*. https://doi.org/10.2514/6.2021-1002

Pocock, C. (2012). *Rheinmetall Shows New Hybrid UAV*. https://www.ainonline.com/aviation-news/defense/2012-09-21/rheinmetall-shows-new-hybrid-uav

Prochazka, K. F., Ritz, T., & Eduardo, H. (2019). Over-Actuation Analysis and Fault-Tolerant Control of a Hybrid Unmanned Aerial Vehicle. *5th CEAS Conference on Guidance, Navigation and Control*.

Sadeghzadeh, I. (2015). *Fault Tolerant Flight Control of Unmanned Aerial Vehicles. PhD Thesis* [PhD's Thesis]. Concordia University.

Sadeghzadeh, I., & Zhang, Y. (2011). A Review on Fault-Tolerant Control for Unmanned Aerial Vehicles (UAVs). *Infotech@Aerospace 2011*. https://doi.org/10.2514/6.2011-1472

Saeed, A. S., Younes, A. B., Cai, C., & Cai, G. (2018). A survey of hybrid Unmanned Aerial Vehicles.

*Progress in Aerospace Sciences*, *98*, 95. https://doi.org/10.1016/j.paerosci.2018.03.007

Saeed, A. S., Younes, A. B., Islam, S., Dias, J., Seneviratne, L., & Cai, G. (2015). A Review on the Platform Design, Dynamic Modeling and Control of Hybrid UAVs. *2015 International Conference on Unmanned Aircraft Systems (ICUAS)*. https://doi.org/10.1109/ICUAS.2015.7152365

Team, T. S. P. R. (2022). *Textron Systems' Aerosonde UAS Begins Operations for Nigeria*. https://www.textronsystems.com/our-company/news-events/articles/press-release/textron-systems-aerosonde-uas-begins-operations

Technologies, B. (2024). *Bayraktar kalkan VTOL*. https://baykartech.com/en/uav/bayraktar-diha/

V. I. Utkin, K. D. Y. (1979). Methods for construction of discontinuity planes in multidimensional variable structure systems. *Autom. Remote Control*, *39*(10), 1466–1470.

Varlık, A., & Erdönmez, M. (2020). Yapılaşmış Alanlarda İnsansız Hava Araçları ile Eğik Resim Fotogrametrisi Uygulaması. *Necmettin Erbakan University Journal of Science and Engineering*, *2*(2), 1–11. https://dx.doi.org/10.47112/neufmbd.2020.1

Wisk. (2024). *Generations 4 and 5*. https://wisk.aero/generations/

Yu, S., & Kwon, Y. (2017). Development of VTOL Drone for Stable Transit Flight. *Journal of Computer and Communications*, *5*, 66–43. https://doi.org/10.4236/jcc.2017.57004

Zhou, L., Si, C., & Wu, Y. (2023, January). Linear Parameter-Varying Control for a Hybrid Unmanned Aerial Vehicle. *AIAA SCITECH 2023 Forum*. https://doi.org/10.2514/6.2023-1046